

Controllable Synthesis of Calcium Carbonate with Different Geometry: Comprehensive Analysis of Particle Formation, Cellular Uptake, and Biocompatibility

Hani Bahrom,^{†,‡,◆} Alexander A. Goncharenko,^{§,◆} Landysh I. Fatkhutdinova,^{||} Oleksii O. Peltek,^{||} Albert R. Muslimov,^{⊥,♯} Olga Yu. Koval,^{⊥,Ⓛ} Igor E. Eliseev,^{⊥,Ⓛ} Andrey Manchev,^{†,‡} Dmitry Gorin,[∇] Ivan I. Shishkin,^{||,Ⓛ} Roman E. Noskov,^{†,‡,Ⓛ} Alexander S. Timin,^{*,§,Ⓛ,Ⓛ} Pavel Ginzburg,^{†,‡} and Mikhail V. Zyuzin^{*,||,Ⓛ}

[†]Department of Electrical Engineering, Tel Aviv University, 55 Haim Levanon Street, Tel Aviv, 69978, Israel

[‡]Light-Matter Interaction Centre, Tel Aviv University, 55 Haim Levanon Street, Tel Aviv 69978, Israel

[§]Peter The Great St. Petersburg Polytechnic University, Polytechnicheskaya str. 29, St. Petersburg, 195251, Russia

^{||}Faculty of Physics and Engineering, ITMO University, Lomonosova str. 9, 191002 St. Petersburg, Russia

[⊥]St. Petersburg Academic University, Khlopina str. 8, 194021 St. Petersburg, Russia

[♯]I. P. Pavlov State Medical University of St. Petersburg, Lev Tolstoy str. 6/8, 197022 St. Petersburg, Russia

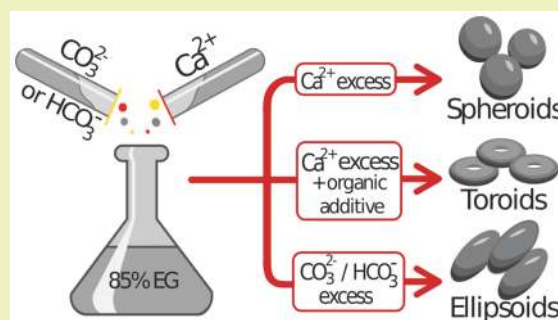
[∇]Skolkovo Institute of Science and Technology, Nobelya str. 3, 121205 Moscow, Russia

[Ⓛ]Research School of Chemical and Biomedical Engineering, National Research Tomsk Polytechnic University, Lenin ave. 30, 634050 Tomsk, Russia

Supporting Information

ABSTRACT: Carefully designed micro- and nanocarriers can provide significant advantages over conventional macroscopic counterparts in drug delivery applications. For the successful delivery of bioactive compounds, carriers should possess a high loading capacity, triggered release mechanisms, biocompatibility, and biodegradability. Porous calcium carbonate (CaCO_3) is one of the most promising platforms, which can encompass all the aforementioned requirements. Here, we study both the formation of particles and the biological applicability of CaCO_3 . In particular, differently shaped anisotropic CaCO_3 particles are synthesized using a sustainable and green approach based on coprecipitation of calcium chloride and sodium carbonate/bicarbonate at different ratios in the presence of organic additives. The impact of salt concentrations, reaction time, and organic additives are systematically investigated to achieve a controllable and reliable design of CaCO_3 particles. It is demonstrated that the crystallinity (vaterite or calcite phase) of particles depends on the initial salt concentrations. The loading capacity of prepared CaCO_3 particles is determined by their surface properties such as specific surface area, pore size, and zeta-potential. Differently shaped CaCO_3 particles (spheroids, ellipsoids, and toroids) are exploited, and their uptake efficiency on an example of C6 glioma cells is evaluated. The results show that ellipsoidal particles are more likely to be internalized by cancer cells. All the particles tested are also found to have good biocompatibility. The ability to design physicochemical properties of CaCO_3 particles has a significant impact on drug delivery applications since particle geometry substantially affects cell behavior (internalization and toxicity).

KEYWORDS: Calcium carbonate, Formation mechanisms, Drug carriers, Adsorption, Cell uptake, Toxicity



INTRODUCTION

Nano- and microparticles are used extensively as a delivery platform for biologically active compounds. Useful functions of particles include controllable physicochemical properties, enhanced loading capacity, high stability in biological fluids, feasibility of incorporation of hydrophilic and hydrophobic compounds, and sustained drug release.^{1–5} Compared to conventional polymer or lipid carriers, the unique characteristics of inorganic nanoparticles can enhance their potential for use in

theranostic applications in both disease therapy and simultaneous bioimaging.⁵

Among widely used inorganic materials, calcium carbonate (CaCO_3) has broad biomedical applications owing to its availability, low cost, safety, biocompatibility, pH-sensitivity,

Received: August 29, 2019

Revised: November 4, 2019

Published: November 6, 2019

and biodegradability.⁶ CaCO_3 has three known natural crystalline forms, vaterite, calcite, and aragonite, the first one being a metastable polycrystal.⁷ Vaterite has caught the attention of the scientific community owing to its peculiar optical and biochemical properties,^{8,9} which include porosity and metastability along with practically relevant, straightforward, and low-cost self-assembly synthesis. Therefore, vaterite particles can be used effectively as biocompatible containers for delivering therapeutic relevant compounds into living cells and tissues.¹⁰ Moreover, CaCO_3 particles can be successfully employed as templates for synthesis of polymer hollow capsules made by using a layer-by-layer method, which are also commonly used as drug delivery carriers.^{11–14}

Several protocols of vaterite synthesis have been reported. For example, the process of crystallization of CaCO_3 occurring through the formation and further transformation of amorphous CaCO_3 into vaterite and then calcite has been demonstrated.¹⁵ The Ostwald ripening process of crystal growth was shown to replace spherulitic growth of vaterite crystals with the subsequent ripening of vaterite and further calcite formation which is determined by a dissolution–precipitation process.¹⁰ Under normal conditions, vaterite particles undergo phase transition into calcite form in aqueous solutions, since the thermodynamic stability of vaterite is lower than that of calcite.^{16,17} Such transition occurs naturally over time, since recrystallization in solution provides possible kinetic paths for the transformation of vaterite crystals into more energetically stable forms of calcium carbonate.^{17,18} One can control the crystallinity of the resultant CaCO_3 particles, as well as their size, shape, and porosity, by changing the synthetic conditions, such as pH values, reagent ratio,^{19,20} temperature,^{21,22} or viscosity of the reaction^{23,24} or by adding organic and inorganic additives.^{25–27} Also, the synthesis of CaCO_3 particles of different phases (vaterite, calcite, and aragonite) with control over size and morphology can be performed without additives using a vortex fluidic device. For example, Boulos et al. investigated the influence of high shear forces on the phase behavior of CaCO_3 .²⁸

There are a number of works describing the crystallization of CaCO_3 in different solvents, e.g., low molecular weight alcohols.^{29,30} Viscosity of reaction significantly influences the crystallization of CaCO_3 due to the reduction of diffusion velocity of calcium and carbonate ions. It allows to control of the velocity of nucleation and CaCO_3 polycrystalline growth, which leads to the reduction in size of the synthesized particles. Water-soluble polyethylene glycol, ethylene glycol, or glycerin are considered to be the most suitable organic solvents.¹³

The temperature and water content of the coprecipitation reaction affect the phase composition of the resultant CaCO_3 particles. Lowering the reaction temperature leads to the formation of calcite particles.¹⁸ At room temperature, the reaction product is usually formed in the vaterite polymorph,³¹ whereas increasing the temperature further induces the formation of aragonite particles.³² The effect of the solvent composition and reaction time is related to the recrystallization process. Low or complete absence of water content results in a stabilization of the crystalline phase of CaCO_3 particles, which are formed at the early stages of the synthesis. Therefore, an introduction of organic additives such as ethylene glycol with a higher than 80% concentration in volume leads to the formation of vaterite and calcite phases of CaCO_3 particles in different ratios.^{20,30}

The acidity of the reaction also plays a crucial role in the formation of CaCO_3 particles and is determined by the concentration of carbonate (CO_3^{2-}) ions. Carbonate ion is an anion of dibasic weak carbonic acid. This means that the constants of the acid dissociation of this compound are lower than 1, namely, $\text{p}K_{a1} = 6.35$ and $\text{p}K_{a2} = 10.33$. This is due to the fact that carbonate ions exist in various forms at different pH values.³³

The rate of CaCO_3 formation is accelerated in the presence of increased concentrations of CO_3^{2-} ions, in particular, at $\text{pH} > 10.5$. The crystallization reaction can be controlled (i) by the defined pH values of initial salts (precursors) or (ii) by changing the CO_3^{2-} ions source, e.g., employing carbonate, bicarbonate (HCO_3^-) ions, or bubbling of carbon dioxide or its absorption from the gas-saturated atmosphere.³⁴ The use of a CO_2 solution allows a minimal reaction rate to be achieved although this method is challenging due to its poor reproducibility.

Finally, the ratios of the initial salts used to produce CaCO_3 particles affect the geometrical properties (size and shape) and surface functionalities (charge and hydrophilicity) of the resultant particles. Recently, it has been shown that a high concentration of CO_3^{2-} ions results in the formation of anisotropic rhomboidal and ellipsoidal geometries, while a low concentration leads to the formation of isotropic spherical particles.^{20,35} Despite a number of studies on the synthesis of CaCO_3 particles of different geometries, e.g., toroids,^{36,37} hollow spherical particles,^{38,39} microsponges,⁴⁰ snowflakes,⁴¹ and flowers,^{42,43} the relation between the morphology of the particles (size, shape, surface properties, and so on) and their phase transformation mechanisms was not systematically studied. In particular, knowledge of the mechanism of how CaCO_3 particles are formed enables their further application in various fields, e.g., drug delivery.^{15,44} With regard to biomedical applications, the biocompatibility of drug carrier platforms should be taken into account to avoid unwanted side effects.^{1,45}

In this work, comprehensive and systematic studies on the formation of differently shaped CaCO_3 particles were performed. In particular, the influence of various concentrations of initial reagents, their ratio, reaction time, and the effect of organic additives on the formation of CaCO_3 particles, were investigated. This study also provides structural insights into the formed CaCO_3 particles, verified with the use of scanning electron microscopy (SEM), laser scanning confocal microscopy (CLSM), X-ray diffraction (XRD), Brunauer–Emmett–Teller analysis (BET), thermogravimetric analysis (TGA), and differential scanning calorimetry (DSC). The formation and growth of CaCO_3 particles of different morphologies are discussed in detail. The impact of particle geometry on cellular uptake in qualitative and quantitative terms was also examined. Additionally, the biocompatibility of the particles formed was tested on an example of C6 glioma cells. A schematic illustration of the synthetic steps performed is depicted in Figure 1.

■ EXPERIMENTAL SECTION

Study of the Formation of CaCO_3 Particles. Synthesis of CaCO_3 particles was performed in coprecipitation reaction. To study the formation of the particles, concentrations of salts (CaCl_2 , Na_2CO_3 , or NaHCO_3), salt ratios, reaction times, and introduction of additives were varied. Details of particle synthesis and a full data set are given in the Supporting Information.

Structural Characterization of Particles. Structural characterization and fraction calculations were performed with the use of X-ray diffractometry via measurement of 2D XRD patterns. Data were collected on a Kappa Apex II diffractometer (Bruker AXS) using $\text{Cu K}\alpha$

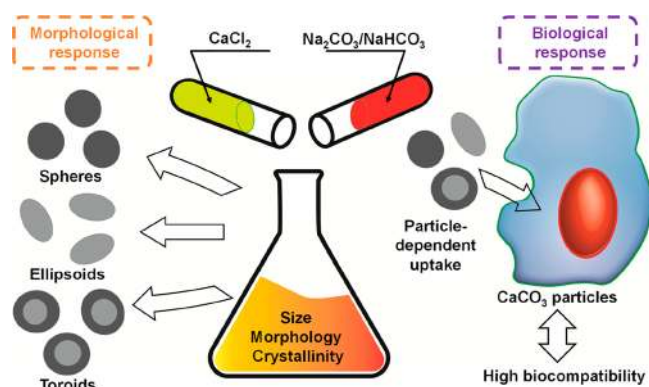


Figure 1. Schematic illustration of the main steps performed to study the process of the formation of differently shaped CaCO_3 particles as well as toxicity and uptake studies.

($\lambda = 1.5418 \text{ \AA}$) radiation generated by a $1\mu\text{S}$ microfocus X-ray tube. 2D images were converted to $\theta-2\theta$ scans using Dioptas software. The crystallite size and phase fraction were calculated by Rietveld refinement using FullProf software package.

The morphology, structure, and size distribution of the particles were determined with the use of scanning electron microscopy (SEM, Quanta200, FEG) at 10 kV acceleration voltage and confocal laser scanning microscopy (CLSM, Carl Zeiss LSM 710). Details of particle synthesis and a full data set are given in the [Supporting Information](#).

Surface Area Characterization of Particles. The BET specific surface area was calculated using adsorption data. Pore size distribution curves were calculated from the analysis of the adsorption branch of the isotherm using the Barrett–Joyner–Halenda algorithm. Errors in determining BET surface areas and pore volumes were estimated to be within 5%.

Thermogravimetric Analysis and Differential Scanning Calorimetry. Thermogravimetric analysis was performed on a TG 209F1 (“Netzsch”, Germany). DSC was carried out using a DSC 204F1 system (“Netzsch”, Germany). Experiments were performed using platinum crucibles in an argon atmosphere with a heating rate of $10 \text{ }^\circ\text{C min}^{-1}$. Accuracy of sample mass measurement was $1 \times 10^{-6} \text{ g}$, and accuracy of temperature measurement was $0.1 \text{ }^\circ\text{C}$.

Dynamic Light Scattering (DLS) and Zeta-Potential Measurements. The zeta potential of particles was measured by DLS which was performed using a Malvern Zetasizer Nano Series running DTS software and operating a 4 mW He–Ne laser at 633 nm. Analysis was performed at an angle of 173° and a constant temperature of $25 \text{ }^\circ\text{C}$.

Adsorption Capacity of Differently Shaped CaCO_3 Particles. The adsorption of dye (TRITC) onto the surface of CaCO_3 particles was measured using a multiplate reader (CLARIOstar, BMG LABTECH). For this purpose, differently shaped particles were incubated with an aqueous solution of TRITC at different concentrations for 2 h. The adsorption capacity was then calculated

and plotted versus the TRITC concentration used. Details of particle synthesis and a full data set are given in the [Supporting Information](#).

Toxicity Studies. Cell viability was measured using LIVE/DEAD assay. For this, cells were fluorescently stained with Calcein AM (for live cells) and Propidium Iodide (for dead cells). Fluorescence images were then taken with CLSM and analyzed with FIJI open source image analysis software. Detailed protocols are presented in the [Supporting Information](#).

Uptake Studies. Internalization of differently shaped CaCO_3 particles was evaluated with CLSM. To this end, TRITC-labeled particles were incubated with C6 glioma cells. The following day, the cytoskeleton of the cells was stained with phalloidin conjugated with AlexaFluor 488, and the cell nuclei were stained with Propidium Iodide. Afterward, the stained C6 glioma cells were scanned with a confocal microscope using the Z-stack option. The indication of intracellular localization of particles was a red signal coming from the fluorescently labeled particles surrounded by a green signal coming from the cell cytoskeleton. The number of internalized cells was then counted and the frequency $f(x)$ histogram of cells, which have internalized x particles per cell, was plotted. Additionally, the cumulative probability $p(x)$ was plotted. Detailed protocols are presented in the [Supporting Information](#).

RESULTS AND DISCUSSION

Calcium Carbonate Particle Formation. The initial focus of this work was aimed at understanding the influence of salt concentrations on the formation of CaCO_3 particles. For this purpose, particles were synthesized by mixing calcium chloride (CaCl_2) with sodium carbonate (Na_2CO_3) at the equal molar ratio (1:1) and varying the initial salt concentrations (CaCl_2 and Na_2CO_3) from 5×10^{-4} to $5 \times 10^{-2} \text{ M}$. The reaction time was 5 min, which refers to the time between the start of the reaction and washing steps. In total, three reactions were performed: reaction $\alpha 1$: $c(\text{CaCl}_2) = 5 \times 10^{-4} \text{ M}$, $c(\text{Na}_2\text{CO}_3) = 5 \times 10^{-4} \text{ M}$; reaction $\alpha 2$: $c(\text{CaCl}_2) = 5 \times 10^{-3} \text{ M}$, $c(\text{Na}_2\text{CO}_3) = 5 \times 10^{-3} \text{ M}$; and reaction $\alpha 3$: $c(\text{CaCl}_2) = 5 \times 10^{-2} \text{ M}$, $c(\text{Na}_2\text{CO}_3) = 5 \times 10^{-2} \text{ M}$. Reaction conditions are listed in [Table S1](#). The size and morphology of the products obtained were further assessed using SEM ([Figure 2](#)). As shown in [Figure 2](#), an increase in salt concentration leads to particle size growth. The product of reaction $\alpha 1$ consisted of amorphous CaCO_3 aggregates. The product of reaction $\alpha 2$ was slightly elongated quasi-spheroidal particles with a size of $519 \pm 89 \text{ nm}$. Finally, the product of reaction $\alpha 3$ was polydispersed particles ranging in size from 500 to 1800 nm. Histograms of particle size distributions are shown in the [Figure S1A](#). By analyzing reactions $\alpha 1$ – $\alpha 3$, we can conclude that reaction $\alpha 2$ is preferable in terms of synthesis of spherical CaCO_3 particles with a narrow size distribution and

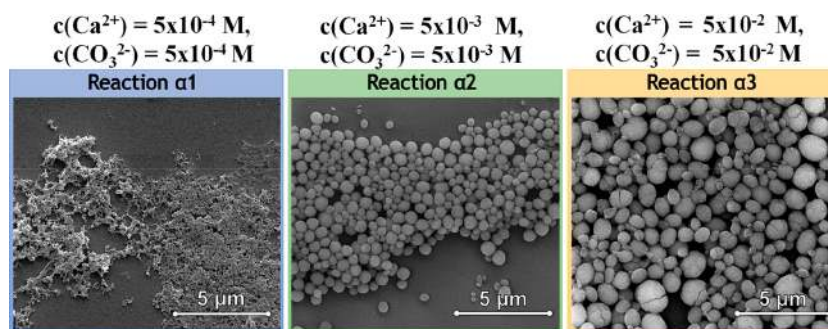


Figure 2. Influence of salts’ concentrations on CaCO_3 particles formation: SEM images of products of reaction $\alpha 1$: $c(\text{CaCl}_2) = 5 \times 10^{-4} \text{ M}$, $c(\text{Na}_2\text{CO}_3) = 5 \times 10^{-4} \text{ M}$; reaction $\alpha 2$: $c(\text{CaCl}_2) = 5 \times 10^{-3} \text{ M}$, $c(\text{Na}_2\text{CO}_3) = 5 \times 10^{-3} \text{ M}$; reaction $\alpha 3$: $c(\text{CaCl}_2) = 5 \times 10^{-2} \text{ M}$, $c(\text{Na}_2\text{CO}_3) = 5 \times 10^{-2} \text{ M}$.

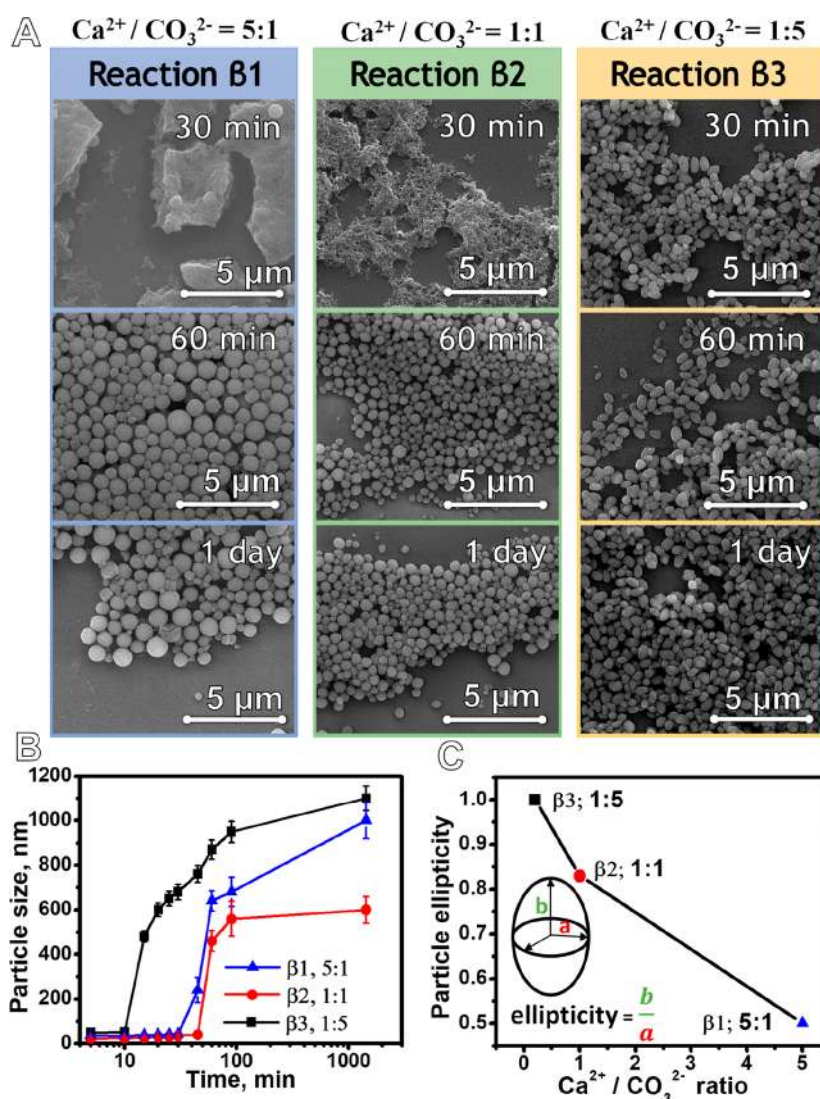


Figure 3. Study of CaCO_3 particle formation kinetics using CaCl_2 and Na_2CO_3 : (A) SEM images of products of reaction β_1 (30 and 60 min and 1 day), reaction β_2 (30 and 60 min and 1 day), reaction β_3 (30 and 60 min and 1 day). (B) Dependence of CaCO_3 particle diameter on reaction time as determined from SEM images. Data are presented as mean \pm standard deviation. (C) Dependence of particle ellipticity on $\text{Ca}^{2+}/\text{CO}_3^{2-}$ ratio.

similar morphology. Therefore, the range of 10^{-3} M was chosen as an optimal value and used in further experiments.

Next, we investigated the process of CaCO_3 particle formation, depending on the reaction time and ion excess concentration. For this purpose, synthesis was performed at various molar salt ratios with reaction times ranging from 5 to 1440 min. To understand the influence of ion excess, the following $\text{CaCl}_2/\text{Na}_2\text{CO}_3$ ratios were used, 5:1, 1:1, and 1:5, resulting in the following: reaction β_1 : $c(\text{CaCl}_2) = 25 \times 10^{-3}$ M, $c(\text{Na}_2\text{CO}_3) = 5 \times 10^{-3}$ M (5:1); reaction β_2 : $c(\text{CaCl}_2) = 5 \times 10^{-3}$ M, $c(\text{Na}_2\text{CO}_3) = 5 \times 10^{-3}$ M (1:1); reaction β_3 : $c(\text{CaCl}_2) = 5 \times 10^{-3}$ M, $c(\text{Na}_2\text{CO}_3) = 25 \times 10^{-3}$ M (1:5). It should be noted that reaction β_2 was not a direct replica of reaction α_2 , since the latter did not include particle growth formation.

SEM images of the resultant products (reactions β_1 – β_3) demonstrate the process of CaCO_3 particle formation over time (Figures 3 and S2). At molar ratios of $\text{CaCl}_2/\text{Na}_2\text{CO}_3 = 1:1$ and 5:1, CaCO_3 particles between 500 and 700 nm in size were observed after 30 min of reaction. A continuous increase in particle size for both ratios was detected. In the case of the molar ratio of 1:5, particle formation had already occurred after 10 min,

and the size of the particles continued to grow up to $\approx 1 \mu\text{m}$. As shown in Figure 3B, an excess of CO_3^{2-} ions accelerates the reaction rate and results in the early stages of CaCO_3 particle formation. For additional verification, XRD analysis of the products from reactions β_1 and β_3 with the reaction time of 20 min was performed (Figure S8). According to the XRD patterns, after 20 min of reaction β_1 , a large fraction of amorphous material was detected, while in the case of reaction β_3 , the peak indicating the amorphous phase was absent. These results are in agreement with SEM analysis and reveal faster formation of crystalline CaCO_3 particles in reaction β_3 . For all tested molar ratios (5:1, 1:1, and 1:5), stable CaCO_3 particles were formed after 1440 min of coprecipitation reaction. Moreover, an excess of Ca^{2+} or CO_3^{2-} ions have an impact on particle geometry. To evaluate this, the ellipticity parameter was used. Analysis of the ellipticity of the particles was performed after 1440 min of coprecipitation reaction. As shown in Figure 3C, at the molar ratio of $\text{CaCl}_2/\text{Na}_2\text{CO}_3 = 5:1$ (reaction β_1), spherical particles were formed. However, a further increase in the concentration of CO_3^{2-} ions resulted in the formation of prolate ellipsoids (particles ellipticity < 1) (Figure 3C). As seen in Figure 3B,C, an

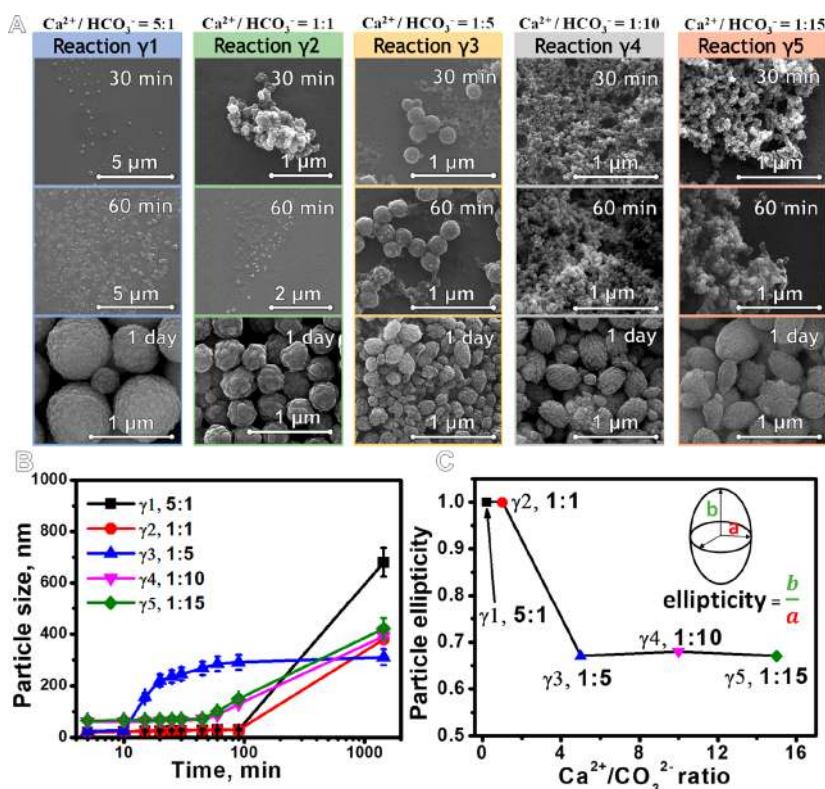


Figure 4. Study of CaCO₃ particle formation kinetics using CaCl₂ and NaHCO₃: (A) SEM images of results of reaction $\gamma 1$ (30 and 60 min and 1 day), reaction $\gamma 2$ (30 and 60 min and 1 day), reaction $\gamma 3$ (30 and 60 min and 1 day), reaction $\gamma 4$ (30 and 60 min and 1 day), reaction $\gamma 5$ (30 and 60 min and 1 day). (B) Particle size of CaCO₃ versus reaction time as determined from SEM images. Data are presented as mean \pm standard deviation. (C) Dependence of particle ellipticity on the Ca²⁺/CO₃²⁻ ratio.

excess of Ca²⁺ ions (reactions $\beta 1$, Ca²⁺/CO₃²⁻ = 5:1) slows down the process of particle formation and promotes the growth of spheroidal particles.

Previous studies revealed that the introduction of HCO₃⁻ ions reduces the reaction rate.²⁷ In this study, NaHCO₃ was used to evaluate the influence of HCO₃⁻ ions.^{33,34} The following reactions γ were carried out: reaction $\gamma 1$: $c(\text{CaCl}_2) = 25 \times 10^{-3}$ M, $c(\text{NaHCO}_3) = 5 \times 10^{-3}$ M; reaction $\gamma 2$: $c(\text{CaCl}_2) = 5 \times 10^{-3}$ M, $c(\text{NaHCO}_3) = 5 \times 10^{-3}$ M; reaction $\gamma 3$: $c(\text{CaCl}_2) = 5 \times 10^{-3}$ M, $c(\text{NaHCO}_3) = 25 \times 10^{-3}$ M; reaction $\gamma 4$: $c(\text{CaCl}_2) = 5 \times 10^{-3}$ M, $c(\text{NaHCO}_3) = 50 \times 10^{-3}$ M; reaction $\gamma 5$: $c(\text{CaCl}_2) = 25 \times 10^{-3}$ M, $c(\text{NaHCO}_3) = 5 \times 10^{-3}$ M. All reaction conditions are listed in Table S1.

In reactions $\gamma 1$ – $\gamma 3$, the same conditions were used as those for reactions $\beta 1$ – $\beta 3$, but NaHCO₃ was used instead of Na₂CO₃. Additionally, reactions $\gamma 4$ and $\gamma 5$ with an increased concentration of HCO₃⁻ were performed to track the formation of particles and their geometry. Reaction times ranged from 5 to 1440 min. Growth of CaCO₃ particles as a function of time was retrieved from SEM images (Figure 4). As expected, the data obtained reveal that the use of HCO₃⁻ reduces the rate of particle growth compared to reactions $\beta 1$ – $\beta 3$. The formation of CaCO₃ particles was observed after 90 min of reaction for all tested molar ratios (5:1, 1:1, 1:10, and 1:15) except 1:5. Particle sizes obtained ranged from 400 to 650 nm after 1440 min. At the molar ratio of 1:5 (reaction $\gamma 3$), the process of particle growth was similar to that in reaction $\beta 3$. In reaction $\gamma 3$, spheroidal particles were already formed after 15 min of reaction. In the case of reactions $\gamma 1$ and $\gamma 2$, the excess of Ca²⁺ ions reduces the rate of particle formation, which supports previous observations (Figure 3B). Additionally, HCO₃⁻ ions delay the formation of

particles. Thus, two factors such as an excess of Ca²⁺ and presence of HCO₃⁻ ions reduce the rate of particle growth.

The product of reaction $\gamma 3$ was particles with heterogeneous morphology containing spheroids and ellipsoids (Figure 4A). This stems from the fact that at the beginning of the reaction (30 and 60 min), spherical CaCO₃ particles were formed due to the dissociation of HCO₃⁻ ions into CO₃²⁻ ions. The presence of dissociated CO₃²⁻ ions with a higher concentration of Ca²⁺ ions reproduces reaction $\beta 1$ (Ca²⁺/CO₃²⁻ = 5:1), which results in the formation of spheroids. However, further dissociation of HCO₃⁻ ions leads to the saturation of CO₃²⁻ ions in solution and shifts the ion balance, which reflects the conditions of reaction $\beta 3$ (Ca²⁺/CO₃²⁻ = 1:5) and promotes the growth of ellipsoids. Thus, a dynamic change of conditions can be responsible for the formation of particles with heterogeneous morphology.

From reactions $\gamma 1$ – $\gamma 5$ which are being considered, reaction $\gamma 3$ appears to be the most suitable because the particles formed in the shortest time. However, the particles obtained possessed heterogeneous morphology. The particles in this sample can be homogenized by varying the initial concentration of HCO₃⁻ ions. To this end, additional reactions $\gamma 6$ and $\gamma 7$ were carried out, where the salt ratio remained the same (CaCl₂/NaHCO₃ = 1:5), but the initial concentrations were increased: reaction $\gamma 6$: $c(\text{CaCl}_2) = 10 \times 10^{-3}$ M, $c(\text{NaHCO}_3) = 50 \times 10^{-3}$ M; reaction $\gamma 7$: $c(\text{CaCl}_2) = 15 \times 10^{-3}$ M, $c(\text{NaHCO}_3) = 75 \times 10^{-3}$ M. SEM images clearly demonstrate the formation of ellipsoidal particles (Figure 5A). According to the results obtained, in the case of reactions $\gamma 3$ and $\gamma 6$, particle growth has a similar reaction rate and induction time (slow rate of chemical reaction). Reaction $\gamma 7$ occurs much faster, as after 10 min stable CaCO₃ particles had already been formed. Thus, the increase in the concentration of

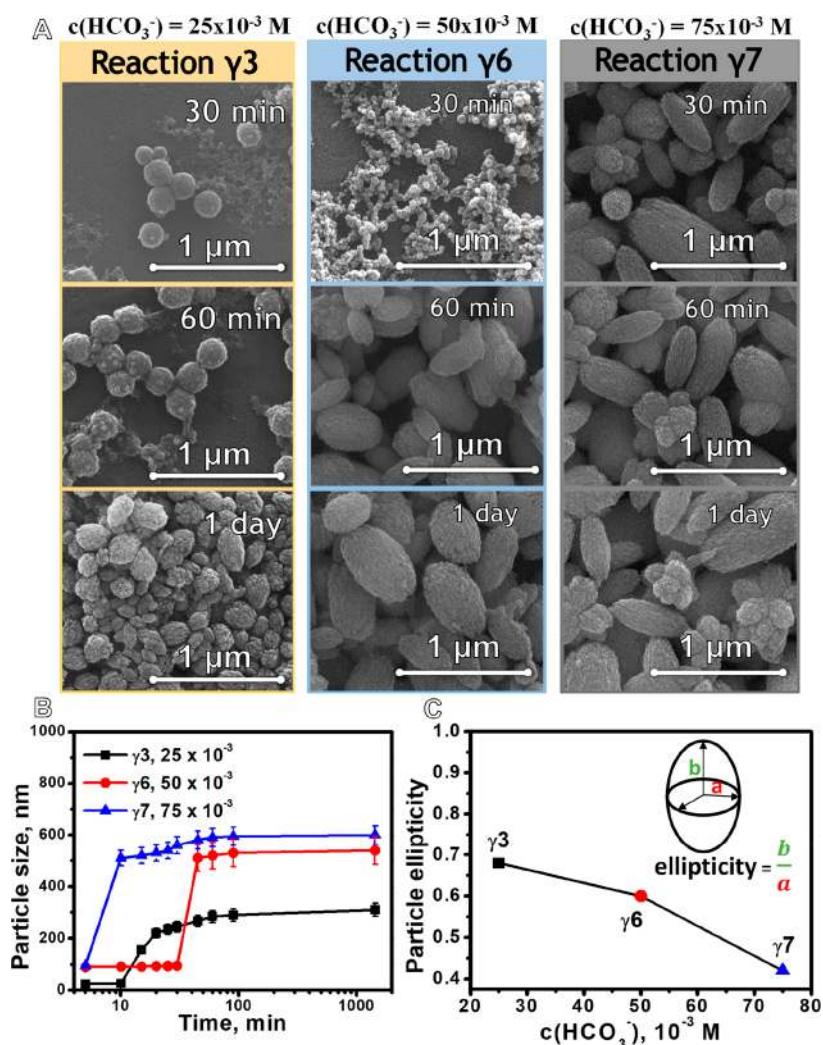


Figure 5. Study of CaCO₃ particle formation using CaCl₂ and NaHCO₃: (A) SEM images of results of reaction γ_3 (30 and 60 min and 1 day), reaction γ_6 (30 and 60 min and 1 day), reaction γ_7 (30 and 60 min and 1 day). (B) Particle size of CaCO₃ versus reaction time as determined from SEM images. (C) Dependence of particle ellipticity on Ca²⁺/CO₃²⁻ ratio. Data are presented as mean \pm standard deviation.

HCO₃⁻ ions resulted in the formation of homogenized ellipsoidal particles with a larger aspect ratio. To sum up, reaction γ_7 results in stable homogenized ellipsoidal particles with particle formation occurring in the shortest time.

Additionally, reactions at ratios of 20:1 and 1:20 were performed (reaction time was 1440 min) to prove that higher concentrations of Ca²⁺ or HCO₃⁻ have an impact on the shape of the particles which are formed. According to the data obtained (Figure S4), at a ratio of 20:1 (Ca²⁺ excess) the slow formation of spheroidal particles was observed, while at a ratio of 1:20 (HCO₃⁻ excess) fast formation of ellipsoids was detected.

To evaluate the influence of molar ratios of CaCl₂ and Na₂CO₃ for reactions β_1 – β_3 and CaCl₂/NaHCO₃ for reactions γ_1 – γ_4 on the calcite/vaterite phase composition, we employed XRD analysis (Figure S7). In the case of reaction β_1 , products were formed that were composed of 55.4% vaterite phase and 44.6% calcite phase (CaCl₂/Na₂CO₃ = 5:1). The same tendency in the phase content was observed for reaction γ_1 , where HCO₃⁻ ions were used (CaCl₂/NaHCO₃ = 5:1). In contrast, in reactions β_2 , β_3 (CaCl₂/Na₂CO₃/NaHCO₃ = 1:1), the percentage of vaterite phase increased up to 85.6 and 84.9%, respectively. The same trend of an increase of vaterite phase was also detected for reactions β_3 , γ_3 , and γ_4 . These results indicate

that an increased concentration of CO₃²⁻ or HCO₃⁻ ions is conducive for the formation of vaterite, while an increased concentration of Ca²⁺ ions results in a high content of calcite phase.

Influence of Organic Additives on CaCO₃ Particle Formation. In order to control the size and shape of CaCO₃ particle formation, organic additives are often used in the coprecipitation reaction.⁴⁶ Charged polymers can interact with Ca²⁺ ions forming Ca–polymer globules and resulting in the formation of metastable amorphous CaCO₃. These metastable complexes define the geometrical parameters of final products.⁴⁷ In this study, dextran sodium sulfate (DS) and poly(styrenesulfonate) sodium (PSS) were used as macromolecular matrices. These organic additives are able to form complexes with Ca²⁺ ions.^{47–49} On the basis of previous data, the 5:1 molar salt ratio resulted in the formation of spheroids (excess Ca²⁺, reaction β_1). Therefore, the same molar ratio of CaCl₂ and Na₂CO₃ (5:1) was used, but with the addition of PSS at different concentrations: reaction δ_1 [$c(\text{CaCl}_2) = 25 \times 10^{-3}$ M, $c(\text{Na}_2\text{CO}_3) = 5 \times 10^{-3}$ M], $c(\text{PSS}) = 0.5$ mg/mL], reaction δ_2 [$c(\text{CaCl}_2) = 25 \times 10^{-3}$ M, $c(\text{Na}_2\text{CO}_3) = 5 \times 10^{-3}$ M], $c(\text{PSS}) = 1$ mg/mL], reaction δ_3 [$c(\text{CaCl}_2) = 25 \times 10^{-3}$ M, $c(\text{Na}_2\text{CO}_3) = 5 \times 10^{-3}$ M], $c(\text{PSS}) = 2$ mg/mL].

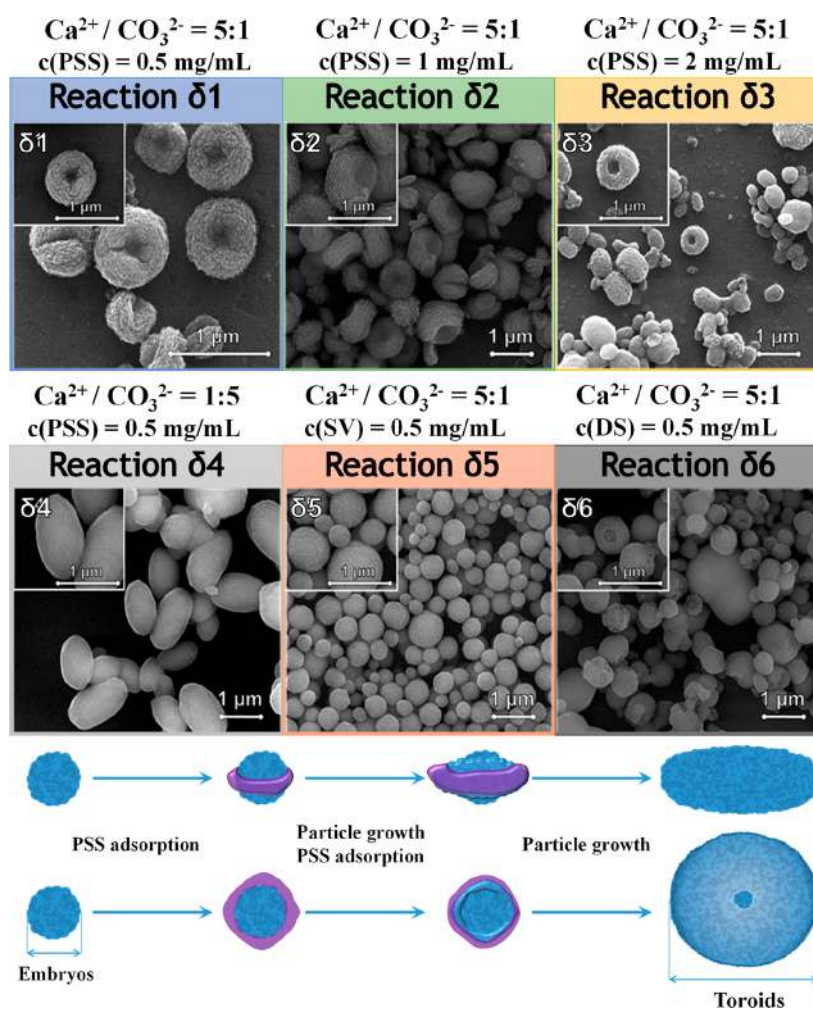


Figure 6. Influence of organic additives on CaCO_3 particle formation. SEM images of products obtained from reactions $\delta 1$ – $\delta 6$ with corresponding schematic illustration of toroid formation by introducing PSS as organic additives.

According to reactions $\delta 1$ – $\delta 3$, particles with unique morphology were formed (Figure 6). The particles obtained had a toroidal-like form with a closed hole in the middle. Similar structures were previously reported, but with larger sizes ($50 \mu\text{m}$ in the ref 36, $5 \mu\text{m}$ in the ref 37, and $1 \mu\text{m}$ obtained in this work). In order to simplify the form of particles obtained and make it clearer for the reader, we refer to the formed CaCO_3 particles as toroids. The toroidal shape of the CaCO_3 particles obtained can be explained by the directional growth of the Ca–polymer globules onto adsorbed polymers. In other words, the adsorbed polymer (PSS) is responsible for the growth of the Ca–polymer globules in the defined direction (Figure 6, scheme). With the highest concentration of PSS (reaction $\delta 3$), polymer is adsorbed onto the CaCO_3 particles forming a dense film predominantly on the toroid's edges and almost absent in the middle of the structure which is formed. With the lowest PSS concentration (reaction $\delta 1$), less polymer is adsorbed onto the edges of the particles formed, resulting in the structure of the obtained toroids being less pronounced. Thus, we found that it is possible to alter the morphology of the final particles by employing various concentrations of PSS.

Next, the influence of organic additives on the formation of CaCO_3 particles with an excess of CO_3^{2-} ions was also studied [reaction $\delta 4$: ($c(\text{CaCl}_2) = 25 \times 10^{-3} \text{ M}$, $c(\text{Na}_2\text{CO}_3) = 5 \times 10^{-3} \text{ M}$), $c(\text{PSS}) = 0.5 \text{ mg/mL}$]. Since the toroids obtained in

reaction $\delta 1$ were more monodispersed, the concentration of PSS 0.5 mg/mL was considered to be the most optimal. In reaction $\delta 4$, ellipsoidal particles were formed. This can be explained by the lack of Ca^{2+} ions, which are needed to form Ca–PSS globules. Therefore, the product of reaction $\delta 4$ was similar to the product of reaction $\beta 3$ without the addition of PSS. Thus, the concentration of Ca^{2+} ions in the coprecipitation reaction affects the geometry and morphology of final products.

In the case of PSS monomers (sodium 4-vinylbenzenesulfonate, SV), the formation of toroidal-like structures was not observed, highlighting that the monomeric structure was not able to guide the growth of the particles in the defined direction (reaction $\delta 5$: $c(\text{CaCl}_2) = 25 \times 10^{-3} \text{ M}$, $c(\text{Na}_2\text{CO}_3) = 5 \times 10^{-3} \text{ M}$, $\text{SV} = 0.5 \text{ mg/mL}$).

Another sulfate-containing polymer, DS, was tested as an example of biodegradable polymer to produce toroidal CaCO_3 particles (reaction $\delta 6$: $c(\text{CaCl}_2) = 25 \times 10^{-3} \text{ M}$, $c(\text{Na}_2\text{CO}_3) = 5 \times 10^{-3} \text{ M}$, $\text{DS} = 0.5 \text{ mg/mL}$). According to the results obtained, the formation of toroidal particles was less pronounced than in the case of PSS as an organic additive. We further investigated the effect of DS concentration on CaCO_3 particle formation (Figure S5). SEM images obtained confirmed that the morphology of the particles obtained did not significantly change according to the DS concentration (0.5 – 2 mg/mL).

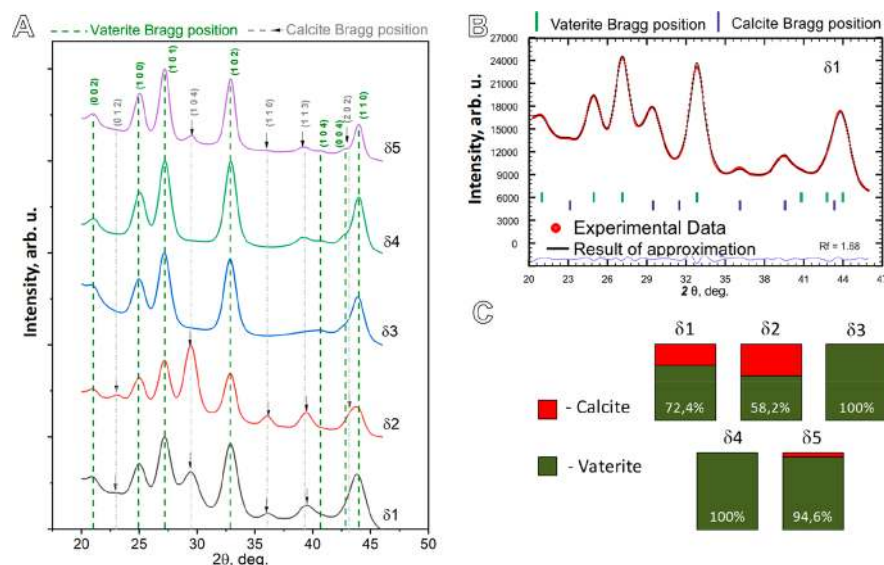


Figure 7. XRD analysis. (A) X-ray powder diffraction patterns of CaCO_3 samples obtained in reactions $\delta 1$ – $\delta 5$. (B) Example of Rietveld fit approximation of powder XRD pattern from CaCO_3 particles obtained in reaction $\delta 1$, where blue bars are calcite Bragg positions, green bars are vaterite Bragg positions, red circles are experimental data, and the black line is the result of approximation. (C) Phase content of CaCO_3 samples obtained in reactions $\delta 1$ – $\delta 5$.

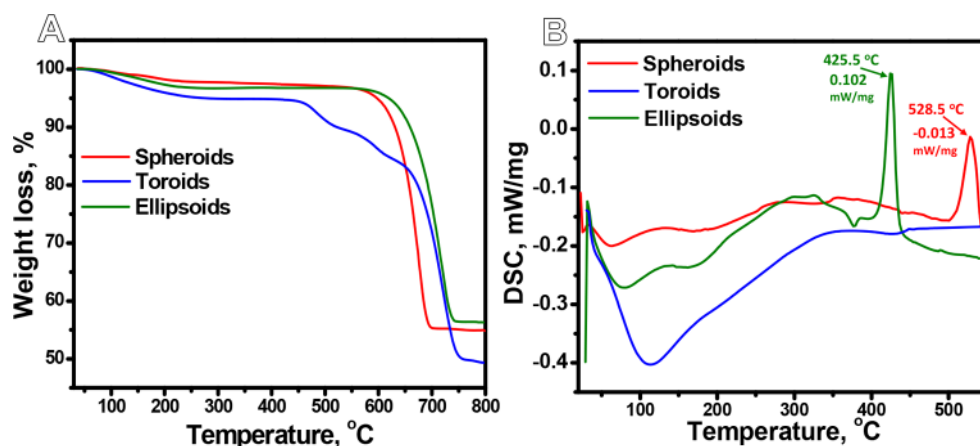


Figure 8. Thermogravimetric analysis and thermal behavior of differently shaped CaCO_3 particles: (A) TGA curves. and (B) DSC curves of spherical (red), toroidal (blue), and ellipsoidal (green) CaCO_3 particles.

Thus, the growth of differently shaped CaCO_3 particles can be controlled by employing organic additives.

XRD analysis was additionally performed to evaluate the phase composition of CaCO_3 particles in the presence of organic additives (Figure 7). According to the data, the addition of PSS into the coprecipitation (reactions $\delta 1$ – $\delta 3$) leads to an increase in vaterite phase compared to reaction $\beta 1$ performed at the same molar ratio ($\text{CaCl}_2/\text{Na}_2\text{CO}_3 = 5:1$ without adding PSS), where vaterite phase was measured to be lower (55%, Figure S7). In the case of reaction $\delta 3$, toroidal particles were formed, which contained 100% vaterite phase, while in reactions $\delta 1$ and $\delta 2$ a mixture of calcite ($R\bar{3}c$)⁵⁰ and vaterite ($P6_3/mmc$)⁵¹ phases was detected (72 and 58%, respectively). Regarding reaction $\delta 4$ ($\text{CaCl}_2/\text{Na}_2\text{CO}_3 = 1:5$, 0.5 mL PSS), we observed the formation of 100% vaterite phase, which can mostly be attributed to excess CO_3^{2-} . We previously demonstrated that an increased concentration of CO_3^{2-} ions is conducive for the formation of vaterite particles (Figure S7). As for reaction $\delta 5$ ($\text{CaCl}_2/\text{Na}_2\text{CO}_3 = 5:1$, 0.5 mL SV), CaCO_3 particles comprising almost 100% vaterite were obtained, indicating that organic monomer

(SV) also stimulates the formation of vaterite particles. The overall data indicate that organic additives (reactions $\delta 1$ – $\delta 5$) in the coprecipitation reaction promote the formation of vaterite phase. These results are in agreement with previously published works.^{52,53} According to these publications, the addition of organic polymers in the coprecipitation reaction stabilizes the amorphous CaCO_3 , preventing and suppressing the mineralization of CaCO_3 .⁵⁴ We then calculated the different sizes of the crystallites from the CaCO_3 particles obtained using the Rietveld refinement method (using FullProf program and the Scherrer equation).^{54–56} The micrometric sized particles which were formed consisted of nanosized crystallite aggregates. Crystallite sizes, as well as lattice volumes are presented in Table S2. The size of the crystalline particles ranged from 8.5 to 20 nm, which results in the difference in surface area and porosity of the CaCO_3 particles obtained.

To summarize all the obtained results on CaCO_3 particle formation, we can distinguish three types of syntheses (reactions $\beta 1$, $\beta 3$, and $\delta 1$), which can lead to the formation of stable CaCO_3 particles of different shapes with comparable sizes: spheroids,

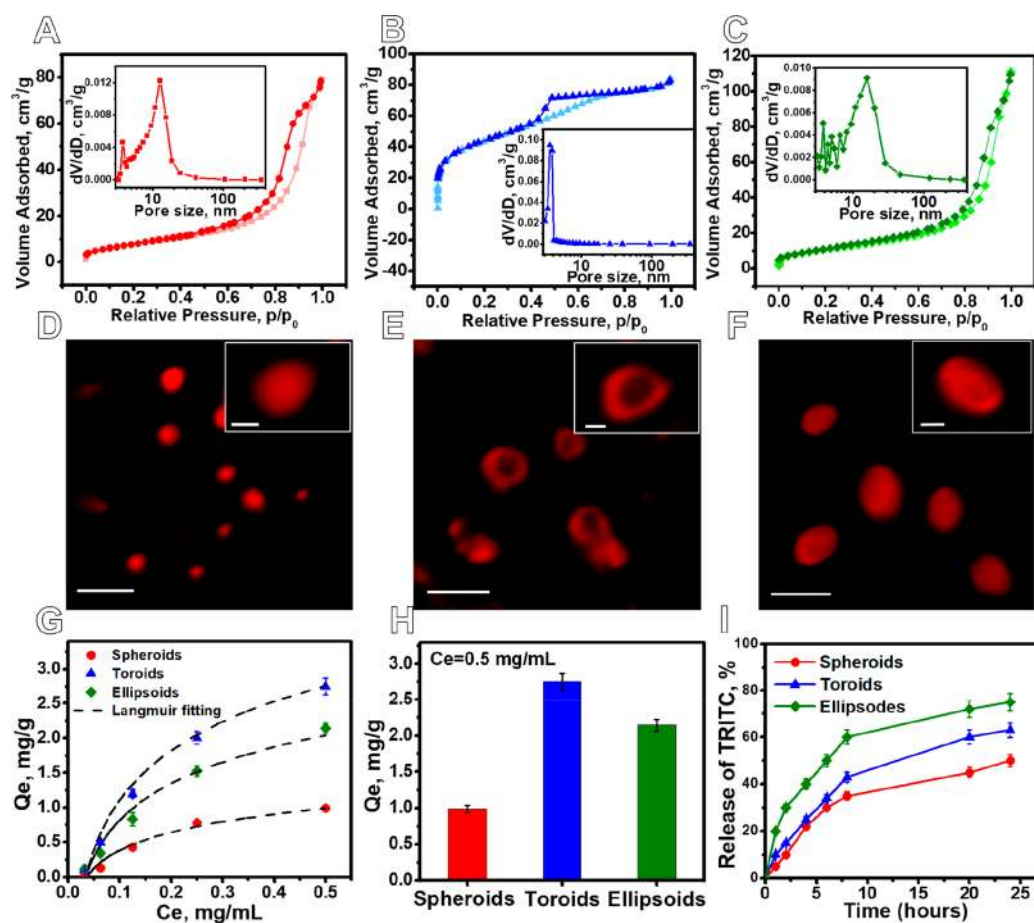


Figure 9. Surface properties of differently shaped CaCO_3 particles with corresponding adsorption/release efficiency: Nitrogen adsorption–desorption isotherms and corresponding pore-size distribution curves (inserts): spheroids (A), toroids (B), and ellipsoids (C). CLSM images of TRITC labeled CaCO_3 particles: spheroids (D), toroids (E), and ellipsoids (F). Scale bars: D–F: $1 \mu\text{m}$, inserts 200 nm (data are presented as mean \pm standard deviation). (G) Nonlinear fits of adsorption isotherm curves for TRITC adsorption of spherical (red), toroidal (blue), and ellipsoidal (green) CaCO_3 particles. (H) Adsorption capacities of spherical (red), toroidal (blue), and ellipsoidal (green) CaCO_3 particles incubated with TRITC at concentration $C_e = 0.5 \text{ mg/mL}$. (I) Percentage of TRITC released from spherical (red), toroidal (blue), and ellipsoidal (green) CaCO_3 particles shaken in water over time (0–24 h).

ellipsoids, and toroids. Therefore, these differently shaped CaCO_3 particles were used for further experiments (Figure S9).

Thermogravimetric Analysis and Thermal Behavior of Differently Shaped CaCO_3 Particles. Next, we investigated the thermal decomposition process of spheroidal, toroidal and ellipsoidal CaCO_3 particles (reactions β_1 , β_3 , and δ_1) by thermogravimetric analysis (TGA), and their thermal behavior was also analyzed by differential scanning calorimetry (DSC). TGA curves of the samples are presented in Figure 8A. According to the results, it is clear that the decomposition process of spheroidal and ellipsoidal CaCO_3 particles (synthesis without organic additives) was similar, while the thermal destruction of toroidal CaCO_3 particles (synthesis in the presence of 0.5 mg/mL PSS) differed from spheroidal and ellipsoidal CaCO_3 particles. The one slight weight loss at $45\text{--}120 \text{ }^\circ\text{C}$ for all three samples resulted from the loss (removal) of physically adsorbed water from CaCO_3 . Furthermore, at $580\text{--}750 \text{ }^\circ\text{C}$, spheroidal and ellipsoidal CaCO_3 particles continued to lose weight, which can be attributed to the decomposition (calcination) of CaCO_3 to CaO and CO_2 (54% of weight loss for spheroids and 56% for ellipsoids). Decomposition of both spheroids and ellipsoids started at around $580 \text{ }^\circ\text{C}$. However, in the case of spheroids, the loss weight finished at $690 \text{ }^\circ\text{C}$, while for ellipsoids it stopped at $720 \text{ }^\circ\text{C}$. Decomposition of both

spheroids and ellipsoids started at around $580 \text{ }^\circ\text{C}$. However, in the case of spheroids, the weight loss finished at $690 \text{ }^\circ\text{C}$, while for ellipsoids it stopped at $720 \text{ }^\circ\text{C}$. The decomposition process of toroids included an additional two phases at $410\text{--}520 \text{ }^\circ\text{C}$ and $550\text{--}650 \text{ }^\circ\text{C}$, which are mostly due to thermal degradation of PSS (organic additives) in a CaCO_3 structure. Indeed, the TGA curve of pure PSS has similar trends in weight loss between 400 and $650 \text{ }^\circ\text{C}$ (Figure S10). Due to the presence of organic additives, the final weight loss of toroidal particles containing PSS was 48%.

The influence of synthetic conditions and organic additives (PSS) on the thermal behavior of differently shaped CaCO_3 particles was studied further using DSC analysis (Figure 8B). DSC curves were measured in the range from 30 to $600 \text{ }^\circ\text{C}$. According to the data obtained, spheroidal and ellipsoidal CaCO_3 particles showed two distinct thermal transitions. The first broad endothermic transition is assigned to the release of physically adsorbed water from the particles.⁵⁷ A first broad peak with a maximum of approximately $100\text{--}120 \text{ }^\circ\text{C}$ was observed for all three types of particles (spheroidal, ellipsoidal, and toroidal) and was more pronounced for the toroidal CaCO_3 particles. This can be attributed to the larger amount of water adsorbed onto the toroidal particles, which can be due to the presence of PSS. The exothermic process at $530 \text{ }^\circ\text{C}$ for spheroids and $420 \text{ }^\circ\text{C}$

for ellipsoids corresponds to the transformation of disordered amorphous CaCO_3 into ordered CaCO_3 crystals (crystallization).⁵⁸ The difference in temperature of exothermic peaks for spheroidal and ellipsoidal CaCO_3 particles can be associated with differences in the size and shape of the particles, which is in agreement with previous work.⁵⁹ Indeed, Zou et al. demonstrated the importance of particle size on the thermal stability and crystallization of amorphous calcium carbonate.⁵⁹ Interestingly, the exothermic peak, which corresponds to crystallization process of CaCO_3 , was absent in case of toroidal particles (synthesis was performed in the presence of organic additive, PSS) in the same temperature range as for spheroids and ellipsoids. This result indicates the inhibition effect of PSS on the crystallization of calcium carbonate under thermal conditions. Xu-Rong et al. showed the same tendency, where PSS inhibits the crystallization of calcium carbonate under thermal conditions and shifts the exothermic peak to temperatures higher than 600 °C.⁶⁰

Surface Area Characterization, Adsorption Capacity of Differently Shaped CaCO_3 Particles, and Release Efficiency. The differently shaped CaCO_3 particles obtained can be employed as carriers for delivery of bioactive compounds; therefore, information about specific surface area is of great importance. Nitrogen isotherms with their corresponding pore-size distribution of differently shaped CaCO_3 particles (reactions $\beta 1$, spheroids; $\beta 3$, ellipsoids; $\delta 1$, toroids) are presented in Figure 9A–C. According to IUPAC classification,⁶¹ spheroids and ellipsoids correspond to type V adsorption/desorption profiles, while toroids correspond to type IV. Hysteresis loops were observed for all types of particles. The hysteresis loop is usually associated with the filling and emptying of mesopores by capillary condensation. The form of hysteresis loops for ellipsoidal and spheroidal CaCO_3 particles corresponds to type H1 (IUPAC classification).⁶¹ In this case, particles exhibit a narrow range of uniform mesopores and network effects are minimal.⁶² This is in contrast to the hysteresis loops of type H2, which correspond to toroidal particles. Type H2 is characterized by more complex pore structures in which network effects are important.

BET surface areas of all samples along with their total pore volumes and average pore sizes calculated using BJH methods are listed in Table 1. The results obtained show that spheroids

Table 1. Surface Properties of Differently Shaped CaCO_3 Particles

	surface area, m^2/g	pore volume, cm^3/g	pore diameter, nm	zeta-potential, mV
spheroids	40.6	0.127	12.7	−2
toroids	75.5	0.084	3.57	−12
ellipsoids	43.1	0.172	15.7	−0.8

are characterized by the lowest specific surface area (40.6 m^2/g) compared to those of ellipsoids (43.1 m^2/g) and toroids (75.5 m^2/g). The increased surface area of toroidal particles can be attributed to the inclusion of PSS in CaCO_3 particles, which can locate on the surface of particles and contribute to their porosity. The organic additive (PSS) can also be a reason for the decreased average pore size of toroidal particles (3.57 nm) compared to those of spheroidal and ellipsoidal particles (12.7 and 15.7 nm, respectively), which can be explained by the filling of pores by PSS resulting in the reduction of the average pore size.

Next, we investigated the adsorption properties (Q_e) of such particles using a physical adsorption approach, which is widely used for the loading of sensitive biomolecules.^{15,63} This is essential for further application of the developed carrier as drug delivery carriers, especially in the case of low molecular weight cargo, since most commercially available drugs are small molecules (under 1000 Da).^{64,65} To estimate the adsorption efficiency of low molecular weight dye (TRITC), the same mass of spheroidal, toroidal and ellipsoidal CaCO_3 particles (reactions $\beta 1$, $\beta 3$, and $\delta 1$) was incubated with TRITC at different concentrations ranging from 0.5 to 0.03 mg/mL. Adsorption isotherm curves were then plotted (Figure 9G). The corresponding CLSM images of differently shaped particles obtained with adsorbed TRITC are depicted in Figure 9D–F. The Langmuir fitting was used to analyze the experimental adsorption isotherms, depicted with the following equation:⁶⁶

$$Q_e = \frac{Q_{\max} bC}{1 + bC} \quad (1)$$

where b is the Langmuir isotherm constant, Q_{\max} is the theoretical monolayer saturation capacity of the TRITC, and C is the equilibrium concentration of TRITC. A detailed description of the calculation of the adsorption capacity of differently shaped CaCO_3 particles is presented in Supporting Information section 7.

From the Langmuir isotherms, it can be seen that even with the smallest concentration of TRITC, the loading capacity of toroidal CaCO_3 particles is higher than that of ellipsoidal and spheroidal particles (Figure 9H). With the maximum added adsorbent concentration (0.5 mg/mL), the adsorption capacity of toroids is 1.2 times higher than the adsorption capacity of ellipsoids and 3 times higher than the adsorption capacity of spheroids. This can be attributed to the surface properties of the resultant particles, which is in agreement with ref 67. Adsorption of TRITC onto porous CaCO_3 particles mainly occurs due to the nonspecific interactions of dye molecules with the CaCO_3 porous surface.⁶⁸ Moreover, electrostatic forces are also involved in the adsorption process, since the TRITC molecules are positively charged. The negatively charged PSS embedded into the structure of toroidal particles (reaction $\delta 1$) eventually contributes to the more negative zeta-potential (−12 mV), compared to those of spheroids and ellipsoids (−2 and −0.8 mV). As a result, the positively charged TRITC is adsorbed onto the surface of toroids at the higher rate due to electrostatic interactions.⁴⁶ Moreover, toroids possess a higher surface area compared to spheroids and ellipsoids, what can also affect the enhanced adsorption capacity of these particles.⁶⁷

To evaluate the release abilities of differently shaped TRITC labeled CaCO_3 particles (spheroidal, toroidal, and ellipsoidal), they were shaken in water for 24 h. At specific time points (1, 2, 4, 6, 8, 20, and 24 h), the amount of released cargo was measured, and the percentage of released TRITC was plotted versus the time of incubation (Figure 9I). The release of TRITC from toroids demonstrated a slightly lower release rate than from ellipsoids, whereas spheroidal particles showed the lowest. The release kinetics for all three types of particles was approximately the same. There is a clear deceleration of cargo release after 10 h of shaking.

Desorption (release) of TRITC molecules from the CaCO_3 particles occurs due to the possible recrystallization of vaterite into calcite in the aqueous solution.²³ As shown earlier in ref 23, exposure of nonmodified vaterite to water media results in complete transition of vaterite into calcite, which possesses a

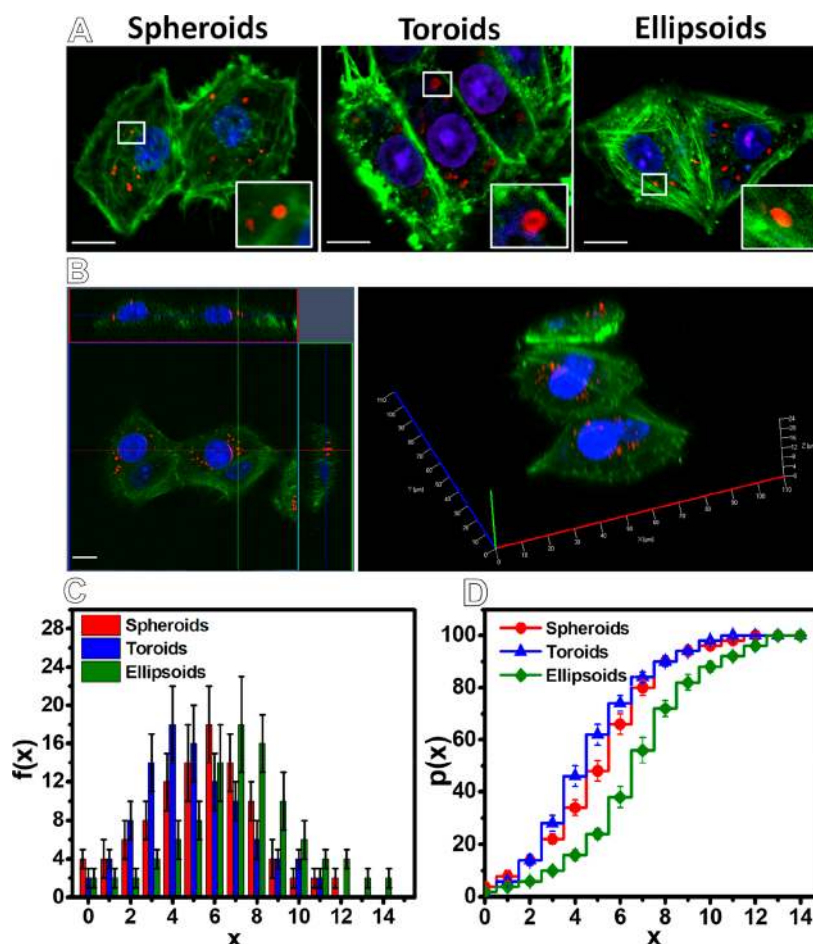


Figure 10. Influence of particle shape on internalization efficiency: (A) CLSM images of C6 glioma cells with internalized particles labeled with TRITC added at cell-to-particle ratio = 1:10. Nuclei: stained blue with PI; Membrane: stained green with phalloidin-AF488; CaCO_3 particles stained red are labeled with TRITC. (B) Z-stack CLSM image confirming the internalization of spherical particles labeled with TRITC with corresponding 3D reconstruction image of cells with internalized particles. (C) Histograms of the frequency $f(x)$ of cells which have internalized x particles per cell after 24 h of incubation with particles at cell-to-particle ratio = 1:10. (D) Corresponding cumulative probability plot $p(x)$ for x internalized particles per cell. Scale bars: (A, B) $10 \mu\text{m}$ (data are presented as mean \pm standard deviation).

lower surface area. The results obtained confirm that the differently shaped CaCO_3 particles are able to adsorb and release bioactive molecules for at least 24 h.

Particle-Dependent Uptake by C6 Glioma Cells. The influence of particle geometry on cellular uptake is extremely important for the further consideration of such carriers in drug delivery. The number of internalized particles per cell was evaluated after 24 h of incubation by counting the particles inside the cells via CLSM and subsequent image analysis. C6 glioma cells were used as a model of a tumor to study cellular uptake efficiency. An incubation period of 24 h was used since different internalization kinetics, and different endocytic processes can proceed differently. Therefore, a longer incubation period ensured that the particle shape was only one parameter influencing the efficiency of uptake.³⁵ The cytoskeleton of cells was fluorescently stained using phalloidin conjugated with AlexaFluor488 (AF488), and cell nuclei were stained with Propidium iodine (PI). The colocalization of TRITC-labeled particles within the cellular compartments was examined using Z-stack option. Figure 10A shows CLSM images of C6 glioma cells that had internalized the differently shaped particles. Figure 10B depicts the three-dimensional CLSM image of a cell scanned from the glass slide to the top of the cell

at different focal distances along the z-axis. The main panel of Figure 10B shows the fluorescent image in the x - y cross section at a given z-location. The two smaller panels reveal the side views of the cell along the x - z (top panel) and y - z cross sections (right side panel). It can be seen that the TRITC labeled particle (red) is located between two layers of fluorescently labeled cell membrane (green). 3D reconstruction of the cell was also performed using conventional ZEN 2009 software (Figure 10B, right). As shown in Figure 10B, red-stained particles are clustered near the cell nucleus in a coplanar position. From the obtained Z-stack images, the frequency $f(x)$ of cells which have internalized x particles per cell and the corresponding cumulative probability $p(x)$ were calculated and depicted in histograms (Figure 10C,D). As shown in Figure 10C,D, toroidal particles were internalized to a lower extent than spheroidal and ellipsoidal particles, while ellipsoidal particles were taken up at significantly higher rate with C6 glioma cells, which is in agreement with previous studies.³⁵ The increased penetration ability of ellipsoidal particles can be attributed to the following. First, the studied particles were mainly internalized with C6 cells via endocytosis,^{44,69} and depending on the shape of the particles, the endocytosis efficiency was different. Second, the contact angle between the particles and the cell membrane, as well as the local curvature of the particle at the contact point with the cell,

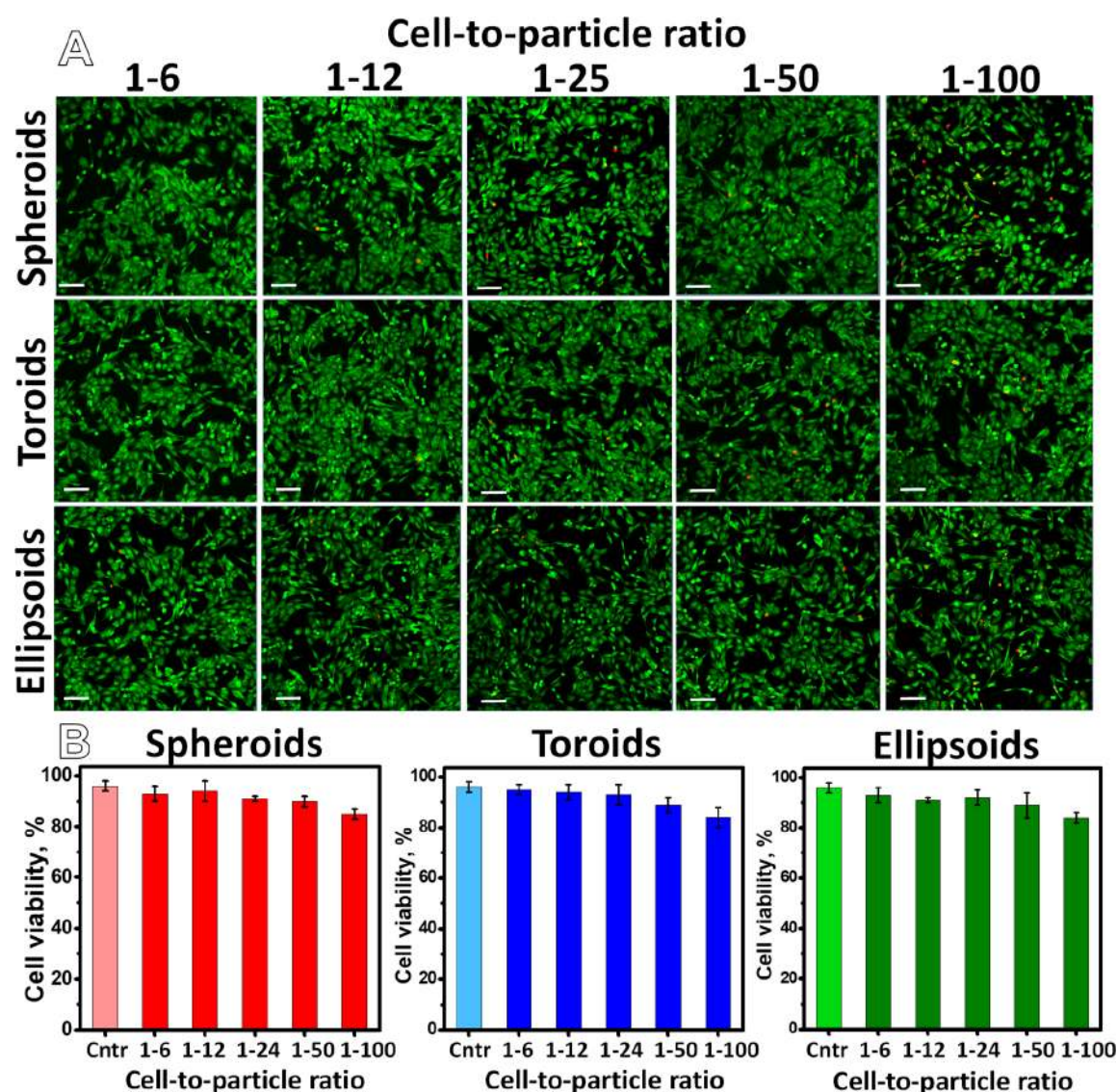


Figure 11. Cytotoxicity of differently shaped CaCO_3 particles: (A) CLSM images of C6 glioma cells incubated with differently shaped CaCO_3 particles at various cell-to-particle ratios for 24 h. Living cells were stained with Calcein AM (green), and dead cells were stained with PI (red). (B) C6 glioma cells viability after incubation with differently shaped CaCO_3 particles. Scale bars: (A, B) 100 μm (data are presented as mean \pm standard deviation).

play a key role in the internalization efficiency of particles. In the case of ellipsoidal particles, the contact angle between the particles and the cell membrane is lower than for spheroidal and toroidal particles. Therefore, it appears that the internalization process of ellipsoids requires less energy of vesicles which wraps the particles and results in a more efficient uptake.⁷⁰ Finally, the decreased local mean curvature at the side edge of ellipsoidal particles assists the uptake of particles.⁷¹ The results obtained are of great importance in the development of shape specific targeting carriers. For example, Kolhar et al. demonstrated that rod-shaped particles showed greater accumulation in organs compared to spheres *in vivo*.⁷²

Evaluation of Particle Toxicity. The toxicity of differently shaped particles at various cell-to-particle ratios of 1:6, 1:12, 1:25, 1:50, and 1:100 was also evaluated on a C6 glioma cell model (Figure 11). For this, differently shaped particles were incubated with cells for 24 h, and then LIVE/DEAD assay was performed. As shown in Figure 11, the viability experiments displayed the absence of cytotoxicity of differently shaped

particles (spheroids, ellipsoids and toroids) even at the highest cell-to-particle ratio (1:100).

The toxicity data obtained are in agreement with previously published data measured on HeLa carcinoma cells.⁶ Zhang et al. evaluated the biological safety of porous CaCO_3 particles on HeLa cells and demonstrated the biocompatibility of CaCO_3 particles in micrometer and nanometer ranges.⁶ Calcium is a key element in cell metabolism. Cells possess mechanisms of tolerance to calcium, as well as effective calcium efflux through calcium channels. Therefore, while fluctuations of calcium ions can influence cell functions (adhesion, moving, signaling, and action potential transduction), the cytotoxic action of sustained released Ca^{2+} on cells is not observed.

CONCLUSIONS

We performed a comprehensive study showing how different physicochemical parameters such as salt concentrations, salt ratios, reaction times, and organic additives can influence the formation of CaCO_3 particles of different geometries and sizes. The data which was obtained revealed that the crystallinity of the

resultant CaCO₃ particles depends on reaction conditions and plays an important role in the surface properties of CaCO₃ particles, colloidal behavior and the phase stability of particles. Such variations in reaction conditions (reactions $\beta 1$, $\beta 3$, and $\delta 1$) allow the formation of differently shaped CaCO₃ particles (spheroids, ellipsoids, and toroids) for further investigation of loading capacity and interaction with cells. Changes in the anisotropy of CaCO₃ particles leads to different adsorption capacities of low molecular weight bioactive compounds. In particular, toroidal-shaped particles are characterized by the highest adsorption capacity compared to spheroids and ellipsoids. The solubility of drug delivery carriers should be also taken into account. As shown in the last study, CaCO₃ particles with the dominant vaterite phase possess increased solubility in biological fluids.⁷³ The outstanding surface properties of these CaCO₃ particles together with their solubility enables them to be used as drug delivery carriers. Therefore, these particles were further used to study the uptake efficiency on an example of C6 glioma cells. As demonstrated, cell uptake depended on the shape of the CaCO₃ particles. Ellipsoids were internalized by C6 glioma cells at the highest rate. Moreover, the differently shaped CaCO₃ particles used did not show any cytotoxic effects even at 100 particles added per cell. As mentioned above, CaCO₃ particles are widely used as carriers for drug delivery due to their nontoxicity, biocompatibility, and degradability in biological fluids. Synthesis of CaCO₃ particles allows carriers to be obtained with different physicochemical properties, e.g., size, shape, morphology, and so forth. It is worth noting that even uncoated vaterite particles, which are not stable in water, can be used as drug delivery carriers, since after the initial contact of the particles with biological fluids, organic compounds tend to bind to the surface of the particles forming a so-called “protein corona” around them. This corona can also stabilize the particles in biological fluids preventing their unwanted mineralization.⁷⁴ The development of differently shaped carriers can be regarded as a prospective drug delivery system, which can eventually lead to a suitable platform for carrying various bioactive compounds.

■ ASSOCIATED CONTENT

📄 Supporting Information

The Supporting Information is available free of charge on the ACS Publications website at DOI: [10.1021/acssuschemeng.9b05128](https://doi.org/10.1021/acssuschemeng.9b05128).

Other experimental results, description of the synthesis of CaCO₃ particles and their characterization using SEM and XRD; procedure for adsorption capacity measurements and drug release study; cell studies, e.g., cell uptake and toxicity (PDF)

■ AUTHOR INFORMATION

Corresponding Authors

*E-mail: a_timin@mail.ru, timin@tpu.ru (A.S.T.).

*E-mail: mikhail.zyuzin@metalab.ifmo.ru (M.V.Z.).

ORCID

Olga Yu. Koval: 0000-0002-1370-474X

Igor E. Eliseev: 0000-0002-3344-2513

Ivan I. Shishkin: 0000-0002-2330-0159

Roman E. Noskov: 0000-0002-9752-8527

Alexander S. Timin: 0000-0002-0276-7892

Mikhail V. Zyuzin: 0000-0002-5364-2635

Author Contributions

◆ H.B. and A.A.G. contributed equally to this work.

Notes

The authors declare no competing financial interest.

■ ACKNOWLEDGMENTS

The work related to cargo encapsulation and delivery carriers characterization was funded by RFBR according to the research project no. 19-015-00098 (A.R.M.). The work related to biological studies of delivery carriers was supported by the Russian Science Foundation, grant no. 19-75-10010 (A.S.T.). The work related to XRD measurements was supported by the Ministry of Education and Science of the Russian Federation, grant no. 16.2593.2017/8.9. M.V.Z. is grateful for the Presidents Scholarship SP-1576.2018.4. This work was supported in part by ERC StG “In Motion” and the PAZY Foundation.

■ REFERENCES

- (1) Zyuzin, M. V.; Díez, P.; Goldsmith, M.; Carregal-Romero, S.; Teodosio, C.; Rejman, J.; Feliu, N.; Escudero, A.; Almendral, M. J.; Linne, U.; et al. Comprehensive and Systematic Analysis of the Immunocompatibility of Polyelectrolyte Capsules. *Bioconjugate Chem.* **2017**, *28* (2), 556–564.
- (2) Kantner, K.; Rejman, J.; Kraft, K. V. L.; Soliman, M. G.; Zyuzin, M. V.; Escudero, A.; del Pino, P.; Parak, W. J. Laterally and Temporally Controlled Intracellular Staining by Light-Triggered Release of Encapsulated Fluorescent Markers. *Chem. - Eur. J.* **2018**, *24* (9), 2098–2102.
- (3) Timin, A. S.; Gao, H.; Voronin, D. V.; Gorin, D. A.; Sukhorukov, G. B. Inorganic/Organic Multilayer Capsule Composition for Improved Functionality and External Triggering. *Adv. Mater. Interfaces* **2017**, *4* (1), 1600338.
- (4) Timin, A. S.; Gould, D. J.; Sukhorukov, G. B. Multi-Layer Microcapsules: Fresh Insights and New Applications. *Expert Opin. Drug Delivery* **2017**, *14* (5), 583–587.
- (5) Zyuzin, M. V.; Timin, A. S.; Sukhorukov, G. B. Multilayer Capsules Inside Biological Systems: State-of-the-Art and Open Challenges. *Langmuir* **2019**, *35* (13), 4747–4762.
- (6) Maleki Dizaj, S.; Barzegar-Jalali, M.; Zarrintan, M. H.; Adibkia, K.; Lotfipour, F. Calcium Carbonate Nanoparticles as Cancer Drug Delivery System. *Expert Opin. Drug Delivery* **2015**, *12* (10), 1649–1660.
- (7) Rodriguez-Blanco, J. D.; Shaw, S.; Benning, L. G. The Kinetics and Mechanisms of Amorphous Calcium Carbonate (ACC) Crystallization to Calcite, Viavaterite. *Nanoscale* **2011**, *3* (1), 265–271.
- (8) Christy, A. G. A Review of the Structures of Vaterite: The Impossible, the Possible, and the Likely. *Cryst. Growth Des.* **2017**, *17* (6), 3567–3578.
- (9) Noskov, R. E.; Shishkin, I. I.; Barhom, H.; Ginzburg, P. Non-Mie Optical Resonances in Anisotropic Biomineral Nanoparticles. *Nanoscale* **2018**, *10* (45), 21031–21040.
- (10) Trushina, D. B.; Bukreeva, T. V.; Kovalchuk, M. V.; Antipina, M. N. CaCO₃ Vaterite Microparticles for Biomedical and Personal Care Applications. *Mater. Sci. Eng., C* **2014**, *45*, 644–658.
- (11) Antipina, M. N.; Sukhorukov, G. B. Remote Control over Guidance and Release Properties of Composite Polyelectrolyte Based Capsules. *Adv. Drug Delivery Rev.* **2011**, *63* (9), 716–729.
- (12) Delcea, M.; Möhwald, H.; Skirtach, A. G. Stimuli-Responsive LbL Capsules and Nanoshells for Drug Delivery. *Adv. Drug Delivery Rev.* **2011**, *63* (9), 730–747.
- (13) Parakhonskiy, B. V.; Yashchenok, A. M.; Konrad, M.; Skirtach, A. G. Colloidal Micro- and Nano-Particles as Templates for Polyelectrolyte Multilayer Capsules. *Adv. Colloid Interface Sci.* **2014**, *207*, 253–264.
- (14) Xue, B.; Kozlovskaya, V.; Sherwani, M. A.; Ratnayaka, S.; Habib, S.; Anderson, T.; Manuvakhova, M.; Klampfer, L.; Yusuf, N.;

Kharlampieva, E. Peptide-Functionalized Hydrogel Cubes for Active Tumor Cell Targeting. *Biomacromolecules* **2018**, *19* (10), 4084–4097.

(15) Trofimov, A.; Ivanova, A.; Zyuzin, M.; Timin, A. Porous Inorganic Carriers Based on Silica, Calcium Carbonate and Calcium Phosphate for Controlled/Modulated Drug Delivery: Fresh Outlook and Future Perspectives. *Pharmaceutics* **2018**, *10* (4), 167.

(16) Cartwright, J. H. E.; Checa, A. G.; Gale, J. D.; Gebauer, D.; Sainz-Díaz, C. I. Calcium Carbonate Polymorphism and Its Role in Biomineralization: How Many Amorphous Calcium Carbonates Are There? *Angew. Chem., Int. Ed.* **2012**, *51* (48), 11960–11970.

(17) Spanos, N.; Koutsoukos, P. G. The Transformation of Vaterite to Calcite: Effect of the Conditions of the Solutions in Contact with the Mineral Phase. *J. Cryst. Growth* **1998**, *191* (4), 783–790.

(18) Ogino, T.; Suzuki, T.; Sawada, K. The Formation and Transformation Mechanism of Calcium Carbonate in Water. *Geochim. Cosmochim. Acta* **1987**, *51* (10), 2757–2767.

(19) Yashchenok, A.; Parakhonskiy, B.; Donatan, S.; Kohler, D.; Skirtach, A.; Möhwald, H. Polyelectrolyte Multilayer Microcapsules Templated on Spherical, Elliptical and Square Calcium Carbonate Particles. *J. Mater. Chem. B* **2013**, *1* (9), 1223.

(20) Svenskaya, Y. I.; Fattah, H.; Inozemtseva, O. A.; Ivanova, A. G.; Shtykov, S. N.; Gorin, D. A.; Parakhonskiy, B. V. Key Parameters for Size- and Shape-Controlled Synthesis of Vaterite Particles. *Cryst. Growth Des.* **2018**, *18* (1), 331–337.

(21) Gopi, S.; Subramanian, V. K.; Palanisamy, K. Aragonite–Calcite–Vaterite: A Temperature Influenced Sequential Polymorphic Transformation of CaCO₃ in the Presence of DTPA. *Mater. Res. Bull.* **2013**, *48* (5), 1906–1912.

(22) Chen, J.; Xiang, L. Controllable Synthesis of Calcium Carbonate Polymorphs at Different Temperatures. *Powder Technol.* **2009**, *189* (1), 64–69.

(23) Trushina, D. B.; Sulyanov, S. N.; Bukreeva, T. V.; Kovalchuk, M. V. Size Control and Structure Features of Spherical Calcium Carbonate Particles. *Crystallogr. Rep.* **2015**, *60* (4), 570–577.

(24) Parakhonskiy, B. V.; Haase, A.; Antolini, R. Sub-Micrometer Vaterite Containers: Synthesis, Substance Loading, and Release. *Angew. Chem., Int. Ed.* **2012**, *51* (5), 1195–1197.

(25) Didymus, J. M.; Oliver, P.; Mann, S.; DeVries, A. L.; Hauschka, P. V.; Westbroek, P. Influence of Low-Molecular-Weight and Macromolecular Organic Additives on the Morphology of Calcium Carbonate. *J. Chem. Soc., Faraday Trans.* **1993**, *89* (15), 2891.

(26) Isopescu, R.; Mateescu, C.; Mihai, M.; Dabija, G. The Effects of Organic Additives on Induction Time and Characteristics of Precipitated Calcium Carbonate. *Chem. Eng. Res. Des.* **2010**, *88* (11), 1450–1454.

(27) Cantaert, B.; Kim, Y.-Y.; Ludwig, H.; Nudelman, F.; Sommerdijk, N. A. J. M.; Meldrum, F. C. Think Positive: Phase Separation Enables a Positively Charged Additive to Induce Dramatic Changes in Calcium Carbonate Morphology. *Adv. Funct. Mater.* **2012**, *22* (5), 907–915.

(28) Boulos, R. A.; Zhang, F.; Tjandra, E. S.; Martin, A. D.; Spagnoli, D.; Raston, C. L. Spinning up the Polymorphs of Calcium Carbonate. *Sci. Rep.* **2015**, *4* (1), 3616.

(29) Sand, K. K.; Rodriguez-Blanco, J. D.; Makovicky, E.; Benning, L. G.; Stipp, S. L. S. Crystallization of CaCO₃ in Water–Alcohol Mixtures: Spherulitic Growth, Polymorph Stabilization, and Morphology Change. *Cryst. Growth Des.* **2012**, *12* (2), 842–853.

(30) Flaten, E. M.; Seiersten, M.; Andreassen, J.-P. Polymorphism and Morphology of Calcium Carbonate Precipitated in Mixed Solvents of Ethylene Glycol and Water. *J. Cryst. Growth* **2009**, *311* (13), 3533–3538.

(31) Andreassen, J.-P. Formation Mechanism and Morphology in Precipitation of Vaterite—Nano-Aggregation or Crystal Growth? *J. Cryst. Growth* **2005**, *274* (1–2), 256–264.

(32) Ševčík, R.; Pérez-Estébanez, M.; Viani, A.; Šašek, P.; Mácová, P. Characterization of Vaterite Synthesized at Various Temperatures and Stirring Velocities without Use of Additives. *Powder Technol.* **2015**, *284*, 265–271.

(33) Gebauer, D.; Völkel, A.; Cölfen, H. Stable Prenucleation Calcium Carbonate Clusters. *Science* **2008**, *322* (5909), 1819–1822.

(34) Jimoh, O. A.; Ariffin, K. S.; Hussin, H. B.; Temitope, A. E. Synthesis of Precipitated Calcium Carbonate: A Review. *Carbonates Evaporites* **2018**, *33* (2), 331–346.

(35) Parakhonskiy, B.; Zyuzin, M. V.; Yashchenok, A.; Carregal-Romero, S.; Rejman, J.; Möhwald, H.; Parak, W. J.; Skirtach, A. G. The Influence of the Size and Aspect Ratio of Anisotropic, Porous CaCO₃ Particles on Their Uptake by Cells. *J. Nanobiotechnol.* **2015**, *13* (1), 53.

(36) Jiang, W.; Pacella, M. S.; Athanasiadou, D.; Nelea, V.; Vali, H.; Hazen, R. M.; Gray, J. J.; McKee, M. D. Chiral Acidic Amino Acids Induce Chiral Hierarchical Structure in Calcium Carbonate. *Nat. Commun.* **2017**, *8* (1), 15066.

(37) Guo, X.; Liu, L.; Wang, W.; Zhang, J.; Wang, Y.; Yu, S.-H. Controlled Crystallization of Hierarchical and Porous Calcium Carbonate Crystals Using Polypeptide Type Block Copolymer as Crystal Growth Modifier in a Mixed Solution. *CrystEngComm* **2011**, *13* (6), 2054.

(38) Cai, A.; Xu, X.; Pan, H.; Tao, J.; Liu, R.; Tang, R.; Cho, K. Direct Synthesis of Hollow Vaterite Nanospheres from Amorphous Calcium Carbonate Nanoparticles via Phase Transformation. *J. Phys. Chem. C* **2008**, *112* (30), 11324–11330.

(39) Beuvier, T.; Calvignac, B.; Delcroix, G. J.-R.; Tran, M. K.; Kodjikian, S.; Delorme, N.; Bardeau, J.-F.; Gibaud, A.; Boury, F. Synthesis of Hollow Vaterite CaCO₃ Microspheres in Supercritical Carbon Dioxide Medium. *J. Mater. Chem.* **2011**, *21* (26), 9757.

(40) Walsh, D.; Lebeau, B.; Mann, S. Morphosynthesis of Calcium Carbonate (Vaterite) Microsponges. *Adv. Mater.* **1999**, *11* (4), 324–328.

(41) Wang, H.; Han, Y.; Li, J. Dominant Role of Compromise between Diffusion and Reaction in the Formation of Snow-Shaped Vaterite. *Cryst. Growth Des.* **2013**, *13* (5), 1820–1825.

(42) Fricke, M.; Volkmer, D.; Krill, C. E.; Kellermann, M.; Hirsch, A. Vaterite Polymorph Switching Controlled by Surface Charge Density of an Amphiphilic Dendron-Calix[4]Arene. *Cryst. Growth Des.* **2006**, *6* (5), 1120–1123.

(43) Hu, Q.; Zhang, J.; Teng, H.; Becker, U. Growth Process and Crystallographic Properties of Ammonia-Induced Vaterite. *Am. Mineral.* **2012**, *97* (8–9), 1437–1445.

(44) Lepik, K. V.; Muslimov, A. R.; Timin, A. S.; Sergeev, V. S.; Romanyuk, D. S.; Moiseev, I. S.; Popova, E. V.; Radchenko, I. L.; Vilesov, A. D.; Galibin, O. V.; et al. Mesenchymal Stem Cell Magnetization: Magnetic Multilayer Microcapsule Uptake, Toxicity, Impact on Functional Properties, and Perspectives for Magnetic Delivery. *Adv. Healthcare Mater.* **2016**, *5* (24), 3182–3190.

(45) Gharib, M.; Khalaf, M.; Afroz, S.; Feliu, N.; Parak, W. J.; Chakraborty, I. Sustainable Synthesis and Improved Colloidal Stability of Popcorn-Shaped Gold Nanoparticles. *ACS Sustainable Chem. Eng.* **2019**, *7*, 9834.

(46) Kato, T.; Sugawara, A.; Hosoda, N. Calcium Carbonate–Organic Hybrid Materials. *Adv. Mater.* **2002**, *14* (12), 869–877.

(47) Smeets, P. J. M.; Cho, K. R.; Kempen, R. G. E.; Sommerdijk, N. A. J. M.; De Yoreo, J. J. Calcium Carbonate Nucleation Driven by Ion Binding in a Biomimetic Matrix Revealed by in Situ Electron Microscopy. *Nat. Mater.* **2015**, *14* (4), 394–399.

(48) Geng, X.; Liu, L.; Jiang, J.; Yu, S.-H. Crystallization of CaCO₃ Mesocrystals and Complex Aggregates in a Mixed Solvent Media Using Polystyrene Sulfonate as a Crystal Growth Modifier. *Cryst. Growth Des.* **2010**, *10* (8), 3448–3453.

(49) Nagaraja, A. T.; Pradhan, S.; McShane, M. J. Poly (Vinylsulfonic Acid) Assisted Synthesis of Aqueous Solution Stable Vaterite Calcium Carbonate Nanoparticles. *J. Colloid Interface Sci.* **2014**, *418*, 366–372.

(50) Graf, D. Crystallographic Tables for the Rhombohedral Carbonates. *Am. Mineral.* **1961**, *46* (11–12), 1283–1316.

(51) Kamhi, S. R. On the Structure of Vaterite CaCO₃. *Acta Crystallogr.* **1963**, *16* (8), 770–772.

(52) Wang, C. Control the Polymorphism and Morphology of Calcium Carbonate Precipitation from a Calcium Acetate and Urea Solution. *Mater. Lett.* **2008**, *62* (16), 2377–2380.

(53) Trushina, D. B.; Bukreeva, T. V.; Antipina, M. N. Size-Controlled Synthesis of Vaterite Calcium Carbonate by the Mixing Method:

Aiming for Nanosized Particles. *Cryst. Growth Des.* **2016**, *16* (3), 1311–1319.

(54) Matahwa, H.; Ramiah, V.; Sanderson, R. D. Calcium Carbonate Crystallization in the Presence of Modified Polysaccharides and Linear Polymeric Additives. *J. Cryst. Growth* **2008**, *310* (21), 4561–4569.

(55) Rietveld, H. M. Line Profiles of Neutron Powder-Diffraction Peaks for Structure Refinement. *Acta Crystallogr.* **1967**, *22* (1), 151–152.

(56) Merlini, M.; Artioli, G.; Cerulli, T.; Cella, F.; Bravo, A. Tricalcium Aluminate Hydration in Additivated Systems. A Crystallographic Study by SR-XRPD. *Cem. Concr. Res.* **2008**, *38* (4), 477–486.

(57) Gorna, K.; Hund, M.; Vučak, M.; Gröhn, F.; Wegner, G. Amorphous Calcium Carbonate in Form of Spherical Nanosized Particles and Its Application as Fillers for Polymers. *Mater. Sci. Eng., A* **2008**, *477* (1–2), 217–225.

(58) Xu, X.; Han, J. T.; Kim, D. H.; Cho, K. Two Modes of Transformation of Amorphous Calcium Carbonate Films in Air. *J. Phys. Chem. B* **2006**, *110* (6), 2764–2770.

(59) Zou, Z.; Bertinetti, L.; Politi, Y.; Jensen, A. C. S.; Weiner, S.; Addadi, L.; Fratzl, P.; Habraken, W. J. E. M. Opposite Particle Size Effect on Amorphous Calcium Carbonate Crystallization in Water and during Heating in Air. *Chem. Mater.* **2015**, *27* (12), 4237–4246.

(60) Xu, X.-R.; Cai, A.-H.; Liu, R.; Pan, H.-H.; Tang, R.-K.; Cho, K. The Roles of Water and Polyelectrolytes in the Phase Transformation of Amorphous Calcium Carbonate. *J. Cryst. Growth* **2008**, *310* (16), 3779–3787.

(61) Thommes, M.; Kaneko, K.; Neimark, A. V.; Olivier, J. P.; Rodriguez-Reinoso, F.; Rouquerol, J.; Sing, K. S. W. Physisorption of Gases, with Special Reference to the Evaluation of Surface Area and Pore Size Distribution (IUPAC Technical Report). *Pure Appl. Chem.* **2015**, *87* (9–10), 1051–1069.

(62) Feoktistova, N.; Rose, J.; Prokopović, V. Z.; Vikulina, A. S.; Skirtach, A.; Volodkin, D. Controlling the Vaterite CaCO₃ Crystal Pores. Design of Tailor-Made Polymer Based Microcapsules by Hard Templating. *Langmuir* **2016**, *32* (17), 4229–4238.

(63) Vikulina, A. S.; Feoktistova, N. A.; Balabushevich, N. G.; Skirtach, A. G.; Volodkin, D. The Mechanism of Catalase Loading into Porous Vaterite CaCO₃ Crystals by Co-Synthesis. *Phys. Chem. Chem. Phys.* **2018**, *20* (13), 8822–8831.

(64) Svenskaya, Y.; Parakhonskiy, B.; Haase, A.; Atkin, V.; Lukyanets, E.; Gorin, D.; Antolini, R. Anticancer Drug Delivery System Based on Calcium Carbonate Particles Loaded with a Photosensitizer. *Biophys. Chem.* **2013**, *182*, 11–15.

(65) Dunuweera, S. P.; Rajapakse, R. M. G. Encapsulation of Anticancer Drug Cisplatin in Vaterite Polymorph of Calcium Carbonate Nanoparticles for Targeted Delivery and Slow Release. *Biomed. Phys. Eng. Express* **2018**, *4* (1), No. 015017.

(66) Timin, A.; Romyantsev, E.; Solomonov, A. Synthesis and Application of Amino-Modified Silicas Containing Albumin as Hemoadsorbents for Bilirubin Adsorption. *J. Non-Cryst. Solids* **2014**, *385*, 81–88.

(67) Parakhonskiy, B. V.; Yashchenok, A. M.; Donatan, S.; Volodkin, D. V.; Tessarolo, F.; Antolini, R.; Möhwald, H.; Skirtach, A. G. Macromolecule Loading into Spherical, Elliptical, Star-Like and Cubic Calcium Carbonate Carriers. *ChemPhysChem* **2014**, *15* (13), 2817–2822.

(68) Volodkin, D. CaCO₃ Templated Micro-Beads and -Capsules for Bioapplications. *Adv. Colloid Interface Sci.* **2014**, *207*, 306–324.

(69) Timin, A. S.; Peltek, O. O.; Zyuzin, M. V.; Muslimov, A. R.; Karpov, T. E.; Epifanovskaya, O. S.; Shakirova, A. I.; Zhukov, M. V.; Tarakanchikova, Y. V.; Lepik, K. V.; et al. Safe and Effective Delivery of Antitumor Drug Using Mesenchymal Stem Cells Impregnated with Submicron Carriers. *ACS Appl. Mater. Interfaces* **2019**, *11* (14), 13091–13104.

(70) Liu, Y.; Tan, J.; Thomas, A.; Ou-Yang, D.; Muzykantov, V. R. The Shape of Things to Come: Importance of Design in Nanotechnology for Drug Delivery. *Ther. Delivery* **2012**, *3* (2), 181–194.

(71) Chen, L.; Xiao, S.; Zhu, H.; Wang, L.; Liang, H. Shape-Dependent Internalization Kinetics of Nanoparticles by Membranes. *Soft Matter* **2016**, *12* (9), 2632–2641.

(72) Kolhar, P.; Anselmo, A. C.; Gupta, V.; Pant, K.; Prabhakarandian, B.; Ruoslahti, E.; Mitragotri, S. Using Shape Effects to Target Antibody-Coated Nanoparticles to Lung and Brain Endothelium. *Proc. Natl. Acad. Sci. U. S. A.* **2013**, *110* (26), 10753–10758.

(73) Lauth, V.; Maas, M.; Rezwan, K. An Evaluation of Colloidal and Crystalline Properties of CaCO₃ Nanoparticles for Biological Applications. *Mater. Sci. Eng., C* **2017**, *78*, 305–314.

(74) Sommerdijk, N. A. J. M.; With, G. de. Biomimetic CaCO₃ Mineralization Using Designer Molecules and Interfaces. *Chem. Rev.* **2008**, *108* (11), 4499–4550.